Structural and Magnetic Characterization of ε-Fe$_2$O$_3$

E. Tronc,[1] C. Chanéac, and J. P. Jolivet

Laboratoire de Chimie de la Matière Condensée, U.M.R. C.N.R.S. 7574, Université Pierre et Marie Curie, 4 Place Jussieu, 75252 Paris Cedex 05, France

ε-Fe$_2$O$_3$ dispersed in silica was obtained by heat treating (1400°C) a composite made up of 10-nm particles of γ-Fe$_2$O$_3$ well dispersed in a silica xerogel based on triethoxysilane (molar ratio Fe/Si = 0.17). The ε-Fe$_2$O$_3$ particles were ca. 30 nm in diameter and α-Fe$_2$O$_3$ was present as a minor phase. X-ray and electron diffraction studies established that ε-Fe$_2$O$_3$ is orthorhombic (a = 509.5 pm, b = 878.9 pm, c = 943.7 pm, *Pna2$_1$*) and isomorphous with AlFeO$_3$, GaFeO$_3$, κ-Al$_2$O$_3$, and presumably ε-Ga$_2$O$_3$. Previous data relative to disordered ε-Fe$_2$O$_3$ were analyzed. The hexagonal symmetry, the cell–subcell (a = 292 pm, c = 944 pm) relationship with ordered ε-Fe$_2$O$_3$, and the type of disorder were established. Mössbauer spectroscopic studies showed that orthorhombic ε-Fe$_2$O$_3$ is a noncollinear ferrimagnet. © 1998 Academic Press

INTRODUCTION

Maghemite, γ-Fe$_2$O$_3$, and hematite, α-Fe$_2$O$_3$, are the two well-known polymorphs of ferric oxide. Maghemite is metastable and transforms under heating into hematite, which is thermodynamically stable. In general, no intermediate phase is observed during the thermal treatment of powders, but for particles dispersed in silica matrices (1, 2) we observed ε-Fe$_2$O$_3$ as an intermediate phase.

ε-Fe$_2$O$_3$ has rarely been observed so far. In 1934, Forestier and Guiot-Guillain (3) reported an iron sesquioxide different from α- and γ-Fe$_2$O$_3$. In 1963, Schrader and Büttner (4) obtained the same material, mixed with hematite and maghemite, by vaporizing iron in an electric discharge under oxygen flux. These authors characterized the X-ray diffraction (XRD) pattern, proposed a monoclinic unit cell, and named the material ε-Fe$_2$O$_3$. Walter-Lévy and Quémeneur (5) obtained it, mixed with hematite, by heating a basic sulfate salt. Trautmann and Forestier (6) reported the preparation of pure ε-Fe$_2$O$_3$ by boiling an aqueous mixture of potassium ferricyanide, sodium hypochlorite, and potassium hydroxide and heating the precipitate at 400°C. Using similar conditions, Dézsi and Coey (7)

obtained fine particles giving a simplified XRD pattern, which was attributed to disorder effects. Viart *et al.* (8) recently obtained fine particles of ε-Fe$_2$O$_3$, mixed with hematite, by heating silica xerogels impregnated with a solution of iron nitrate. Transformation of ε-Fe$_2$O$_3$ into hematite under heating was reported to take place at 500–750°C according to the preparation method (3–7). Magnetic studies (4, 6) of the bulk material concluded to ferrimagnetic properties with a Curie temperature of ca. 210°C. A similar ordering temperature and antiferromagnetic properties were reported (7) for the disordered material.

We recently reported (1, 2) the formation of ε-Fe$_2$O$_3$ by heat treatment of γ-Fe$_2$O$_3$ nanoparticles well dispersed in silica xerogels. The composites were prepared by *in situ* polymerization of a silica precursor, silicic acid or triethoxysilane, in an aqueous sol of well-dispersed γ-Fe$_2$O$_3$ nanoparticles. The γ-Fe$_2$O$_3$ nanoparticles in the composites were stable up to at least 1000°C. Heating at higher temperatures yielded α-Fe$_2$O$_3$ as the only iron oxide when the matrix was fully crystallized (into cristobalite) and ε-Fe$_2$O$_3$ as the major iron oxide when crystallization had not occurred or was incomplete. Here, we focus on a composite where ε-Fe$_2$O$_3$ is the major iron oxide. We present the results of a structural and magnetic characterization of this phase by X-ray diffraction, transmission electron microscopy, and Mössbauer spectroscopy experiments. We also present an analysis of the data (7) relative to the disordered material and discuss the structural relationship between the ordered and disordered varieties.

EXPERIMENTAL

1. Materials

The preparation of the γ-Fe$_2$O$_3$–silica composite, triethoxysilane based, has been detailed elsewhere (1,2). Particles of γ-Fe$_2$O$_3$ (Fe^{II}/Fe^{III} ≤ 0.01), ca. 10 nm in diameter, were prepared by coprecipitation of Fe^{III} and Fe^{II} ions and subsequent oxidation in acidic medium (9) forming a stable sol (pH ~ 2) with minimum aggregation of particles (10). Pure triethoxysilane, introduced into the sol, was hydrolyzed and condensed according to the formal

reactions

$$HSi(OCH_2CH_3)_3 + 3H_2O \rightarrow 3CH_3CH_2OH + HSi(OH)_3$$

$$\rightarrow HSiO_{1.5} + 1.5H_2O$$
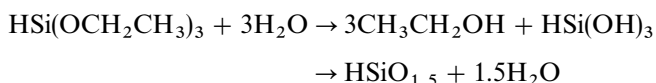
The added amount of alkoxysilane corresponded to the molar ratio Fe/Si = 0.17. Under vigorous stirring, an emulsion formed initially, then a homogeneous solution, and finally a gel after 30 min at room temperature. The ε-Fe$_2$O$_3$–silica composite was obtained by heating the as-dried material under oxygen flux up to 1400°C at the rate of 5°C/min, keeping the temperature at 1400°C for 30 min, and then cooling down to room temperature at the rate of 5°C/min. IR spectroscopic studies gave no evidence of Fe–O–Si bonding.

2. Techniques

The XRD pattern was obtained with a Philips PW1830 powder diffractometer operating in reflection geometry with Cu$K\alpha$ radiation and equipped with a graphite back mono-chromator. The pattern was recorded over the 2θ range from 10° to 80° with a 2θ step size of 0.05° and a scanning rate of 30 s per step. The position, width, and height of the $K\alpha_1$ lines were determined using the Fit Profile subroutine of the Philips APD 3.5 program package. The observed line intensity was taken as the height times the width. The lattice parameters of ε-Fe$_2$O$_3$ were determined from relationships between the d^{-2} values and least-squares refined from the position of 10 single lines under the assumption of orthorhombic symmetry. The line intensities were calculated for various models by means of the CaRine 3.0 program package (11) neglecting the polarization correction due to the monochromator and compared visually to the observed data. The atomic scattering factors of Fe^{3+} and O^{2-} were used, with an average temperature factor, B, of 1×10^4 to 2×10^4 pm^2.

Structural features of the disordered material were deduced by analyzing the data in ref 7. The unit cell and the oxygen arrangement were determined from simple considerations. Iron site occupancies and z positions were refined through a classical least-squares procedure adapted to the treatment of powder lines. The observed line intensities, I_o, were scaled from 10 to 100. All unobserved lines were taken into account with intensity set at 5, giving a total set of 19 lines ($d \geq 105$ pm). As the experimental radiation was unknown, the corrections for Lorentz and polarization effects, applied to the calculated intensities, I_c, were first achieved considering radiations Cu$K\alpha$, Co$K\alpha$, and Fe$K\alpha$. Preliminary refinements yielded $B < 0$ for Cu$K\alpha$, $B > 4 \times 10^4$ pm^2 for Fe$K\alpha$, and $B \approx 2 \times 10^4$ pm^2 for Co$K\alpha$, so the latter was retained. Three models were considered involving $4-11$ variables including a scale factor, K, and an overall B factor.

The K factor, the site occupancies, the z positions, and the B factor were refined successively until convergence was reached (generally after two cycles). The reliability index is given by $R = \sum |I_o - I_c|/\sum I_o$.

Transmission electron microscopy (TEM) observations were performed using a Jeol 100CXII microscope. The composite was examined in the form of thin sections, 80–100 nm thick. The Au diffraction pattern was used to scale the reciprocal lattice.

^{57}Fe Mössbauer spectra were recorded with a conventional spectrometer operating in the sine or linear velocity mode and equipped with a source of ^{57}Co/Rh. In-field experiments were achieved with a magnetic field of 6 T applied parallel to the direction of propagation of the γ-rays. The velocities were calibrated from the spectrum of a foil of α-Fe. The isomer shifts are given relative to α-Fe at room temperature.

RESULTS AND DISCUSSION

Figure 1 shows a TEM image of the ε-Fe$_2$O$_3$–silica composite. The particles are of globular shape, with an average diameter of the order of 30 nm. Figure 2 shows the XRD pattern. It consists of a broad band centered at $2\theta \sim 22°$, produced by the amorphous matrix, a peak at $2\theta = 21.9°$ indicating partial crystallization into cristobalite, and a set of narrow lines whose positions and relative intensities are consistent with a mixture of ε-Fe$_2$O$_3$ (4) and α-Fe$_2$O$_3$. ε-Fe$_2$O$_3$ is the major iron oxide phase, involving ca. 80% of the total iron amount as determined from the Mössbauer study reported herein.

1. Unit Cell of ε-Fe$_2$O$_3$

(a) X-ray diffraction. The characteristics of the ε-Fe$_2$O$_3$ XRD pattern are listed in Table 1 as well as the previous
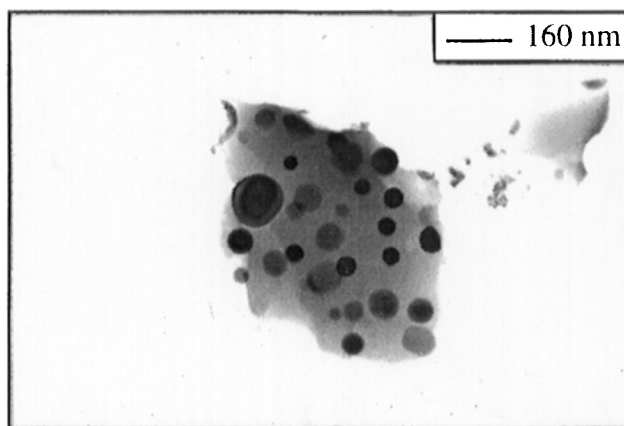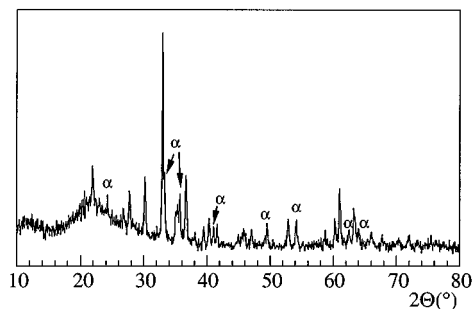

FIG. 1. Transmission electron microscopy image of ε-Fe$_2$O$_3$ particles dispersed in silica (Fe/Si = 0.17).

FIG. 2. X-ray diffraction pattern (CuKα) of ε-Fe₂O₃ particles dispersed in silica (Fe/Si = 0.17). (α-Fe₂O₃ involves ca. 20% of the total iron amount).

data (4–7) ($d \geq 131$ pm). Significant variations in the intensities are observed between the various sets. The present data are somewhat similar to those of Schrader and Büttner (4). A certain number of weak lines excepted, the main differences lie in the line at $d = 166.6$ pm, which we do not observe, and that at $d = 138.3$ pm, which we find much weaker.

Schrader and Büttner (4) proposed a monoclinic unit cell with parameters $a = 1297$ pm, $b = 1021$ pm, $c = 844$ pm, and $\beta = 95.66°$ and assumed content $Z = 20$ Fe₂O₃ formula units. This unit cell is not related in a simple way to the basic parameters of a close-packed arrangement of oxygen ions, unlike for all well-known iron hydroxides, oxyhydroxides, and oxides (12, 13). All known structures derive from a hexagonal, cubic, or mixed hexagonal–cubic close packing of oxygen ions with the iron ions leading, in general, to a superstructure. The unit cell is, therefore, related to the basic vectors of the oxygen ion stacking, namely $\mathbf{a}_{ox}$ and $\mathbf{b}_{ox}$ associated with the average hexagonal unit cell of the two-dimensional (2D) array and $\mathbf{c}_{ox}$ perpendicular to the layers with magnitude, c_{ox}, equal to the average distance between two successive oxygen layers.

Hematite has the corundum structure. The anions are hexagonally close packed. All cations are in octahedral sites. Perpendicularly to the close-packing direction, they form a honeycomb arrangement which shifts from one layer to the other, leading to rhombohedral symmetry ($R\bar{3}c$) over six oxygen layers. The oxygen lattice parameters as deduced from the hexagonal unit cell ($a = 504$ pm, $c = 1375$ pm, $Z = 6$) are $a_{ox} = a/\sqrt{3} = 290$ pm and $c_{ox} = c/6 = 229$ pm. Maghemite is a cation-deficient spinel. The cations occupy octahedral and tetrahedral sites of the cubic close packed arrangement of the oxygen ions, and the vacancies are located in the octahedral sublattice. In general, no sign of vacancy ordering is observed for particles less than ca. 20 nm in diameter (14). Thus the unit cell is cubic ($Fd3m$). Its content may be written as (Fe₈)[Fe₁₃.₃₃◇₂.₆₇]O₃₂ where () and [] stand for tetrahedral and octahedral sites, respectively, and ◇ represents a vacancy. The lattice constant is

$a = 835$ pm. The parameter of the cubic oxygen lattice is twice as small, leading to $a_{ox} = a\sqrt{2}/4 = 295$ pm and $c_{ox} = a\sqrt{3}/6 = 241$ pm.

In view of the slight variations in the values of a_{ox} and c_{ox} between hematite and maghemite, we can expect similar data for ε-Fe₂O₃, i.e., a_{ox} of the order of 290–300 pm and c_{ox} of the order of 230–240 pm.

Disordered form. For the disordered material, Dézsi and Coey (7) reported 11 lines down to $d = 105$ pm. The first line is at $d = 253$ pm, and there are two broad bands at larger d values. All the lines are well indexed (Tables 1 and 2) on the hexagonal unit cell with $a = 292$ pm and $c = 944$ pm; i.e., $a = a_{ox}$ and $c = 4c_{ox}$ with $c_{ox} = 236$ pm. This is typical of a close packing involving four oxygen layers with no superstructure due to the iron ions. The unit cell content is Fe₂.₆₇O₄, neglecting the small degree of hydration or hydroxylation (7). The two broad bands can be indexed as $\frac{11}{22}.1$ ($d = 279$ pm) and $\frac{11}{33}.1$ ($d = 397$ nm), which suggests a cation arrangement at short range involving three basic cells in the [11.0] direction. The smallest suitable 2D supercell is the rectangular cell with $a = a_{ox}\sqrt{3}$ and $b = 3a_{ox}$, defined, for instance, by $\mathbf{a} = \mathbf{a}_{ox} - \mathbf{b}_{ox}$ and $\mathbf{b} = 3(\mathbf{a}_{ox} + \mathbf{b}_{ox})$.

Ordered form. As a matter of fact, the orthorhombic supercell with $a = a_{ox}\sqrt{3}$, $b = 3a_{ox}$, and $c = 4c_{ox}$, allows the interpretation of the other XRD patterns (Table 1), supporting an order–disorder relationship between the materials. Least-squares refinement of our data yielded $a = 509.5(1)$ pm, $b = 878.9(2)$ pm, and $c = 943.7(3)$ pm. The value of c (c_{ox}) is the same as for the disordered structure and that of a_{ox} (~ 293.5 pm) is slightly larger. The volume of the orthorhombic cell is 423×10^6 pm³, ca. 2.5 times smaller than that of the monoclinic cell (4), and the content is Fe₁₆O₂₄ ($Z = 8$). The line indexing suggests that the possible reflections are limited by the conditions $h0l$ with $h = 2n$ and $0kl$ with $k + l = 2n$. These conditions are characteristic of space group $Pna2_1$-C_{2v}^9 (15).

(b) Electron diffraction. A few representative electron diffraction patterns of the particles in the composite are given in Fig. 3. A rectangular lattice is observed in Fig. 3a. The indexing on the (a_{ox}, c_{ox}) hexagonal cell shows that the observed plane is the ($1\bar{2}.0$) plane of a close packing with $\mathbf{c} = 4\mathbf{c}_{ox}$. In Fig. 3b, the ($a_{ox}$, c) hexagonal cell yields the lattice defined by the reflections labeled P and Q, indexed as $1\bar{1}.\bar{2}$ and 10.2, respectively, with R corresponding to 11.6. The extra reflections on the rows parallel to [$1\bar{1}.\bar{2}$] and [10.2] define an orthorhombic superlattice. By indexing P as $20\bar{2}$ and R as 066, the reciprocal and direct unit cells are given by

$$\mathbf{a}^* = \tfrac{1}{2}(\mathbf{a}_{ox}^* - \mathbf{b}_{ox}^*), \quad \mathbf{b}^* = \tfrac{1}{6}(\mathbf{a}_{ox}^* + \mathbf{b}_{ox}^*), \quad \mathbf{c}^* = \tfrac{1}{4}\mathbf{c}_{ox}^*$$

$$\mathbf{a} = \mathbf{a}_{ox} - \mathbf{b}_{ox}, \quad \mathbf{b} = 3(\mathbf{a}_{ox} + \mathbf{b}_{ox}), \quad \mathbf{c} = 4\mathbf{c}_{ox},$$

TRONC, CHANÉAC, AND JOLIVET

TABLE 1
Intensities and Positions (pm) of the X-Ray Diffraction Lines of ε-Fe$_2$O$_3$[a]

hkl	Orthorhombic[b]				Ref 4		Ref 5		Ref 6		Ref 7		Hexagonal[b]	
	I_c^c	d_c	I_o	d_o	I_o	d_o	I_o	d_o	I_o	d_o	I_o	d_o	d_c	hk.l
011	5	643.1			4	647.0	20	643						
002	3	471.8			2	476.0								
111	<1	399.4			2	401.0					bb	400	397	$\frac{1}{3}\frac{1}{3}.1$
120	4	332.8	9	332.6	6	334.0								
112	12	321.6 }												
022	15	322.6 }	24	321.6	20	324.0	30	323	vw	322				
121	3	313.9			4	315.0								
013	33	296.1	34	296.2	35	298.1	60	298	w	296				
031	3	279.8			<1	280.4					bb	280	279	$\frac{1}{2}\frac{1}{2}.1$
122	100	272.0	100	271.8	100	272.8	20	274	s	272				
113	12	256.0	10	256.1	8	257.3								
200	13	254.8 }												
130	8	254.0 }	25	254.1	20	254.8	20	255	m	254	s	253	253	10.0
201	13	246.0 }												
131	27	245.3 }	42	245.1	30	245.8	100	246	m	245	s	244	244	10.1
210	3	244.7 }												
004	5	235.9			4	237.2								
123	10	228.6	12	228.5	6	229.5								
202	4	224.2 }												
132	11	223.6 }	22	223.7	20	224.3	60	224	m	224	s	223	223	10.2
212	14	217.2	11	217.2	14	217.6	10	218						
140	3	201.8	7	201.8	4	201.8								
222	2	199.7 }												
042	5	199.2 }	8	199.2	20	199.7								
203	3	198.0 }												
133	6	197.6 }	10	197.7	20	198.3	30	198	m	198	m	197	197	10.3
141	<1	197.3			12	197.3								
213	8	193.1	9	193.2			20	194						
142	5	185.5			12	185.5								
015	3	184.5	x	184.1										
223	3	180.5			2	180.7								
115	1	173.5 }												
204	9	173.1 }	24	173.2	25	173.5	60	174	m	173	m	173	173	10.4
134, 051	10	172.8 }												
240	2	166.8			25	166.6	10	167						
035, 320	1	158.5			10	158.0								
006, 312	7	157.2	8	157.3	10	157.3								
242	2	156.9			10	156.2								
321	1	156.3												
053, 144	13	153.4	15	153.5	12	153.7	30	154						
205	12	151.7 }												
135	28	151.5 }	43	151.8	35	152.0	100	152	s	151	s	151	151	10.5
322	2	150.2 }												
215, 234	1	149.2 }			5	150.1								
243, 330	22	147.0 }												
060	8	146.45 }	33	146.9	30	146.9	100	147	vs	147	vs	146	146	11.0
323	10	141.3	12	141.5	10	141.6	10	143						
160	2	140.8			2	140.8								
252	9	138.3	7	138.3	80	138.3	20	139						
206	1	133.8 }												
136	1	133.7 }	12	134.1	4	133.9								

TABLE 1—*Continued*

hkl	Orthorhombic[b]				Ref 4		Ref 5		Ref 6		Ref 7		Hexagonal[b]	
	$I_c{}^c$	d_c	I_o	d_o	I_o	d_o	I_o	d_o	I_o	d_o	I_o	d_o	d_c	hk.l
017	2	133.2			2	132.9								
253	4	131.4	10	131.2	6	131.5								

[a] Indexing on orthorhombic ($a = 509.5$, $b = 878.9$, $c = 943.7$ pm) and hexagonal ($a = 292$, $c = 944$ pm) unit cells.

[b] Present study. vs, s, m, w, and vw stand for very strong, strong, medium, weak, and very weak intensity, respectively; bb stands for broad band, and x for overlap with a hematite line.

[c] I_c: intensities calculated using the atomic positions in Ga$_{0.87}$Fe$_{1.13}$O$_3$ (17) (see text).

in accordance with the XRD results. The a, b, and c values are practically in the ratios $\sqrt{2}:\sqrt{6}:\sqrt{7}$, which leads us to identify the observed plane with $(2\bar{6}7)$.

Practically all observed patterns can be analyzed on the orthorhombic unit cell. Complex sets of reflections were generally observed due to tilt effects and interception of reflections slightly above or below the view plane. For example, the view plane in Fig. 3c, close to $(10, 3, \overline{21})$, contains the [061] direction. The [051] and [071] directions, inclined at less than 2° below and above the plane,
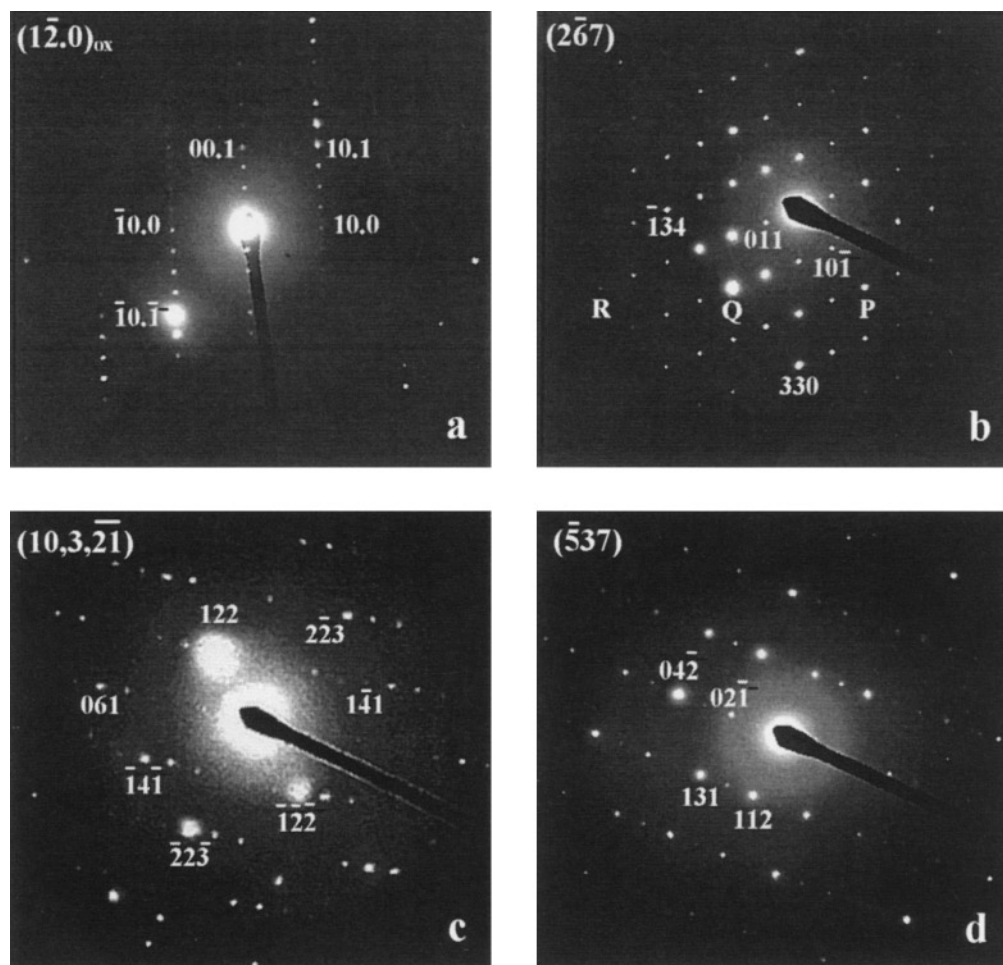
FIG. 3. Electron diffraction patterns of ε-Fe$_2$O$_3$ particles: (a) indexing on the hexagonal cell of a close-packed oxygen arrangement with lattice constant a_{ox} and interlayer spacing c_{ox}; (b) orthorhombic superstructure. P($20\bar{2}$), Q(132), and R(066) belong to the hexagonal sublattice defined by $a = a_{ox}$, $c = 4c_{ox}$ (P: $1\bar{1}.\bar{2}$; Q: 10.2; R: 11.6). (c, d) More complex patterns, orthorhombic indexing.

respectively, lead to the observation of a few reflections separated by $\mathbf{b}^*$, nearly on the rows parallel to [061]. A few patterns suggested a larger cell with doubled b or c, which may result from periodic defects. The latter situation is illustrated in Fig. 3d by additional spots on the rows parallel to [02$\bar{1}$].

No systematic absences were observed. As none are expected for symmetry $Pna2_1$ due to multidiffraction, it is clear that the TEM observations support our analysis of the XRD pattern.

2. Structure of ε-Fe₂O₃

Both hexagonal and orthorhombic structures derive from a close packing of four oxygen layers. Therefore, the stacking is either hexagonal or double-hexagonal. The main structural features can be determined assuming an idealized structure with equally spaced atomic layers and all atoms sitting in A, B, or C sites with (x,y) positions relative to the oxygen cell given by $(0, 0)$, $(\frac{2}{3}, \frac{1}{3})$, and $(\frac{1}{3}, \frac{2}{3})$, respectively. The oxygen stacking is of type $/ABAB/$ or $/ABAC/$. By putting an A oxygen layer at $z = 0$, the octahedral sites are located at $z = (2n + 1)/8$ and the tetrahedral sites at $z = (2n + 1)/16$ with n integer.

(a) Hexagonal form. In the XRD pattern (7) of the disordered material, the first six lines represent the 10.*l* set with $0 \leq l \leq 5$ (Table 1). The intensities are essentially similar for even and odd l values. This cannot be achieved with the $/ABAB/$ stacking assuming that there are no empty oxygen sandwiches and that iron sixfold coordination is preferential, which seems reasonable in view of the γ- and α-Fe₂O₃ structures. Therefore, we conclude that the oxygen stacking is of the $/ABAC/$ type. Four space groups may be considered according to the z position of the equivalent cation sites: $P6_3/mmc$ $(\pm z, \frac{1}{2} \pm z)$, $P6_3mc$ $(z, \frac{1}{2} + z)$, $P\bar{3}m1$ $(\pm z)$, and $P3m1$ (z). Refinements were performed under each of the first three symmetries, the last being discarded because it yielded too many variables. Configurations related by inversion through a symmetry center under $P6_3mc$ or by symmetry through a mirror plane under $P\bar{3}m1$ are equivalent.

Under each of the three considered space groups, the refinement of the octahedral site occupancies with zero occupancy of the tetrahedral sites leads to $R \sim 0.5$. This suggests that tetrahedral sites must be occupied. A site occupancy drastically reduces the 10.0 line whatever the space group and does not allow the R value to decrease significantly, so the relevant tetrahedral sites are likely to be of the (B, C) type. The resulting stacking is represented in Fig. 4 and may be written as

$$/A(\beta c.)B(.c\beta)A(\gamma b.)C(.b\gamma)/A, \quad [1]$$
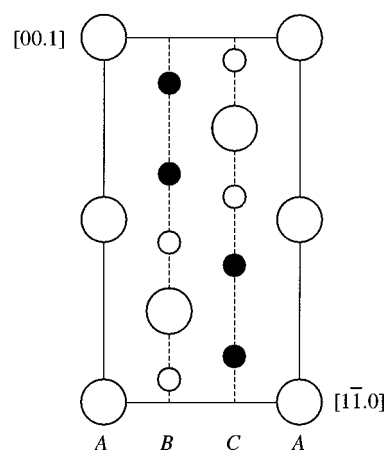

FIG. 4. Structure of disordered ε-Fe₂O₃ [(11.0) section; oxygen (○); iron in octahedral (●) and tetrahedral (○) sites].

where capitals stand for oxygen ions, Roman and Greek lowercase letters for ferric ions in octahedral and tetrahedral sites, respectively, and dots for empty cation layers.

The fit results are reported in Table 2. In each case, the estimated unit cell content is close to the theoretical one, Fe₂.₆₇O₄, which supports our analysis. The model with symmetry $P6_3/mmc$ leads to $R = 0.20$. The I_o and I_c values show some notable discrepancies that can hardly be attributed solely to the poor accuracy of the observed data, which suggests this model is not satisfactory. The models with symmetry $P\bar{3}m1$ and $P6_3mc$ lead to $R = 0.10$ and 0.08, respectively. In both cases, a satisfying agreement between the I_o and I_c values is obtained for all major lines, and slight discrepancies occur only for weak or unobserved lines. The limited accuracy of the observed data makes it difficult to select one of these two models. Following the stacking sequence, the occupancy factors of the cation sites are given by

$P6_3mc$

$$/A(0.40\ 0.25\ 0)B(0\ 0.54\ 0.14)A(0.40\ 0.25\ 0)C(0\ 0.54\ 0.14)/A$$

$$[2]$$

$P\bar{3}m1$

$$/A(0.21\ 0.49\ 0)B(0\ 0.61\ 0.06)A(0.06\ 0.61\ 0)C(0\ 0.49\ 0.21)/A$$

$$[3]$$

The four- to six-coordinated iron stoichiometry is close to 2:3 in [2] and 1:4 in [3]. The difference is significant and could be used to validate one particular model, but we do not know the real ratio. As model [2] leads exactly to the expected iron amount and to a better agreement for both observed and unobserved lines, we tend to conclude that it is more appropriate.

TABLE 2
Structural Refinement of Disordered ε-Fe$_2$O$_3$[a]

d_o (pm)	d_c (pm)		I_o	$hk\cdot l^{a,b}$	I_c^a	I_c^b	I_c^c	$hk.l^c$
	472.0		5	00.2	7	5	10	00.2
253	252.9	s	70	10.0	59	68	67	10.0
244	244.3	s	70	10.1	62	70	70	10.$\pm$1
	236.0		5	00.4	21	8	7	00.4
223	222.9	s	70	10.2	75	72	71	10.$\pm$2
197	197.1	m	50	10.3	51	49	54	10.$\pm$3
173	172.5	m	50	10.4	57	47	50	10.$\pm$4
	157.3		5	00.6	2	3	5	00.6
151	151.3	s	70	10.5	86	71	74	10.$\pm$5
146	146.0	vs	100	11.0	86	103	100	11.0
	139.5		5	11.2	1	<1	1	11.2
	133.6		5	10.6	<1	2	<1	10.$\pm$6
126	$\{$126.4 / 125.3$\}$	vvw	10	$\{$20.0 / 20.1$\}$	11	11	13	$\{$20.0 / 20.$\pm$1$\}$
	124.2		5	11.4	16	9	7	11.4
	122.1		5	20.2	4	3	4	20.$\pm$2
118	$\{$119.0 / 118.0 / 117.3$\}$	vw	20	$\{$10.7 / 00.8 / 20.3$\}$	11	20	12	$\{$10.$\pm$7 / 00.8 / 20.$\pm$3$\}$
112	111.5	vvw	10	20.4	9	8	9	20.$\pm$4
	107.0 / 106.9		5	$\{$11.6 / 10.8$\}$	5	8	145	$\{$11.6 / 10.$\pm$8$\}$
105	105.1	w	30	20.5	24	21	22	20.$\pm$5

Inequivalent site coordinates and occupancy factors.[b]

a: $P6_3/mmc$ O$_1$ 0 0 0; $\frac{1}{2}$ O$_2$ $\frac{2}{3}\frac{1}{3}\frac{1}{4}$; $\frac{1}{2}$ Fe$_1$ $\frac{2}{3}\frac{1}{3}$ 0.092(8); 0.11(1) Fe$_2$ $\frac{1}{3}\frac{2}{3}$ 0.140(2); 0.58(1)

b: $P6_3mc$ O$_1$ 0 0 0; 1 O$_2$ $\frac{2}{3}\frac{1}{3}$ 0.222(11); 1 Fe$_1$ $\frac{2}{3}\frac{1}{3}$ 0.095(9); 0.40(3) Fe$_4$ $\frac{2}{3}\frac{1}{3}$ 0.165(8); 0.25(2)
Fe$_3$ $\frac{2}{3}\frac{2}{3}$ 0.436(20); 0.14(2) Fe$_4$ $\frac{1}{3}\frac{2}{3}$ 0.351(9); 0.54(2)

c: $P\bar{3}m1$ O$_1$ 0 0 0; $\frac{1}{2}$ O$_2$ $\frac{2}{3}\frac{1}{3}$ 0.206(4); 1 Fe$_1$ $\frac{2}{3}\frac{1}{3}$ 0.025(5); 0.21(4) Fe$_2$ $\frac{1}{3}\frac{2}{3}$ 0.159(4); 0.49(2)
O$_3$ 0 0 $\frac{1}{2}$; $\frac{1}{2}$ Fe$_2$ $\frac{2}{3}\frac{1}{3}$ 0.425(30); 0.06(3) Fe$_4$ $\frac{1}{3}\frac{2}{3}$ 0.382(3); 0.61(3)

[a] Observed data from ref 7. vs, s, m, w, vw, and vvw stand for very strong, strong, medium, weak, very weak, and very very weak intensity, respectively.

[b] Standard deviations in parenthesis.

FIG. 5. Projection of the unit cell of ε-Fe$_2$O$_3$ onto (001). Labeling of the $B(z)$ and C ($\frac{1}{2} + z$) sites equivalent in space group $Pna2_1$ is shown.

(b) Ordered structure. Projected onto (001) the orthorhombic unit cell contains six oxygen cells and, hence, six A, B, and C sites as illustrated in Fig. 5. In space group $Pna2_1$, all atoms are in general fourfold position with the coordinates of the equivalent positions given by

$$x, y, z; \tfrac{1}{2} + x, \tfrac{1}{2} - y, z; \bar{x}, \bar{y}, \tfrac{1}{2} + z; \tfrac{1}{2} - x, \tfrac{1}{2} + y, \tfrac{1}{2} + z.$$

The six A, B, or C sites at a distance z split into three pairs which are equivalent to three A, C, or B pairs at $\frac{1}{2} + z$. The oxygen stacking cannot be /ABAB/. It is necessarily /ABAC/, as in the disordered structure (Fig. 4). Since the unit cell content is Fe$_{16}$O$_{24}$, there are four inequivalent cations assuming site occupancies equal to 0 or 1. Since the point group of the oxygen stacking is 6/*mmm* (order 24) and that of the superstructure is *mm*2 (order 4), a given cation
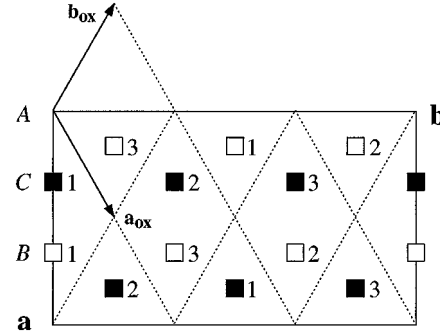
arrangement can take six different relative orientations (there are three ways of orienting the (**a, b**) cell with respect to the (**a**$_{ox}$, **b**$_{ox}$) subcell and, for each of them, two configurations related to one another by inversion through a center of symmetry because the z axis is polar). The six configurations are equivalent regarding powder diffraction.

The good arrangement (and equivalents) can be deduced in a simple way. We consider the idealized close-packed structure with $b/a = \sqrt{3}$. We take the asymmetric unit in the fourth of the unit cell defined by $x < \frac{1}{2}$, $y < 1$, $z < \frac{1}{2}$ and label (Fig. 5) the $C(x, y)$ positions at $(\frac{1}{3}, 0)$, $(\frac{1}{3}, \frac{1}{3})$, and $(\frac{1}{3}, \frac{2}{3})$, C_1, C_2, and C_3, respectively, and, correspondingly, the $B(x, y)$ positions at $(\frac{1}{6}, \frac{1}{2})$, $(\frac{1}{6}, \frac{5}{6})$, and $(\frac{1}{6}, \frac{1}{6})$, B_1, B_2, and B_3. The strongest line in the observed pattern (Table 1, Fig. 2, and Fig. 6a) is the 122 superstructure line. The anions, at idealized positions, do not contribute to this line. The geometrical structure factor is zero for $x = 0(\frac{1}{2})$ or $y = 0(\frac{1}{2})$ so that only the B_2, C_2, B_3, and C_3 cation positions can give a nonzero contribution. The maximum intensity is obtained for the set $B_2(z = \frac{1}{16})$, $C_2(\frac{1}{8})$, $C_3(\frac{3}{8})$, $B_3(\frac{7}{16})$. This set also yields very strong 110 and 020 superstructure lines, which are unobserved. These lines, with low hkl indices, are unlikely to vanish under the sole effect of atomic shifts, so we can reasonably conclude that the foregoing set of positions is not the good one.

The next strong intensity of the 122 line is obtained for a variety of arrangements with one A, B_1, or C_1 position instead of B_2 or B_3. All configurations but one give strong discrepancies for some of the lines at angles lower than 122. The only satisfying set of positions is given by $B_2(z = \frac{1}{6})$, $C_2(\frac{1}{8})$, $C_1C_3(\frac{3}{8})$. The corresponding stacking and the series of the average site occupancies may be written as:

$$/A(\beta_2 c_2.)B(.c_{1,3}.)A(\gamma_2 b_2.)C(.b_{1,3}.)/A$$

$$/A(\tfrac{1}{3}\tfrac{1}{3}0)B(0\tfrac{2}{3}0)A(\tfrac{1}{3}\tfrac{1}{3}0)C(0\tfrac{2}{3}0)/A. \qquad [4]$$

The calculated pattern is represented in Fig. 6b. All notable observed lines (Fig. 6a) have a calculated intensity that is
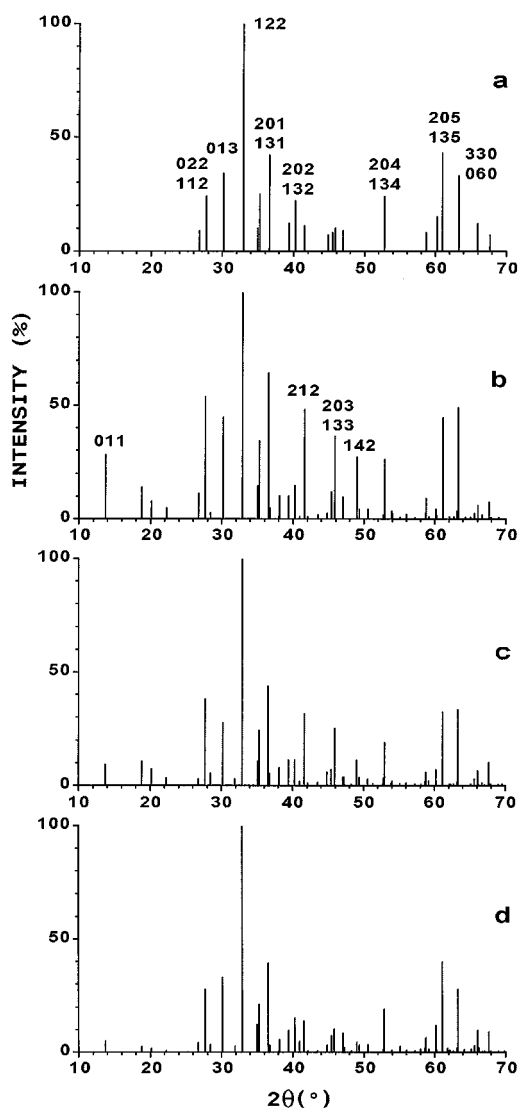
FIG. 6. Schematic X-ray diffraction patterns of ε-Fe_2O_3: (a) observed; (b) calculated for the idealized structure ($b/a = \sqrt{3}$); (c) cation position C_1 shifted by $\Delta y = 0.03$; (d) atomic positions as in $Ga_{0.87}Fe_{1.13}O_3$ (17) (see text).

significant, and there is no unobserved line with very strong calculated intensity. However, the calculated intensity of most fundamental lines (20l, 13l) and some superstructure lines is too strong. Significant improvements (Fig. 6c) can be obtained by slightly changing the y coordinate ($\Delta y = 0.03$) of the C_1 cation site. There are 29 position parameters, so their refinement is likely to yield a fit of very good quality, and we can conclude that the stacking in [4] is the good one.

Figure 7 shows a representation of the idealized structure. The main data are reported in Table 3. The six-coordinated cation located in the oxygen sandwich with mixed occupancy (c_2 in stacking [4]) is named Fe_1, and the two others
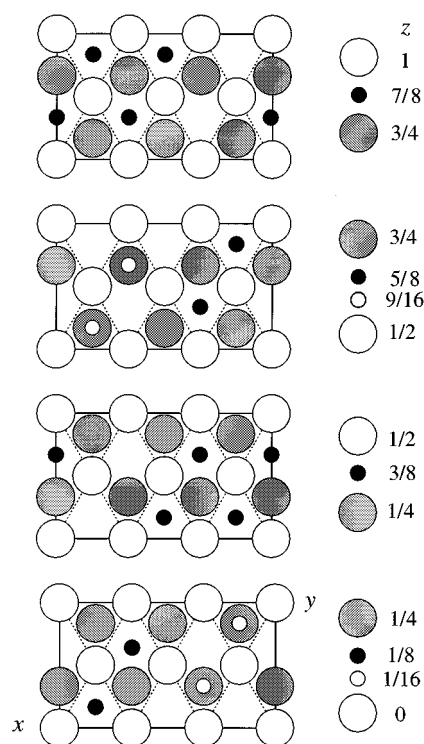
FIG. 7. Schematic representation of the structure of ε-Fe_2O_3, showing the projection of the successive oxygen sandwiches onto (001). [Oxygen in A($\bigcirc$) and B,C ($\bigodot$) sites; iron in octahedral ($\bullet$) and tetrahedral ($\circ$) sites].

Fe_2 (c_1) and Fe_3 (c_3). The four-coordinated cation is named Fe_4. The structure (Fig. 8) consists of triple chains of octahedra sharing edges and simple chains of tetrahedra sharing corners which run parallel to the a direction. The triple chains are linked to one another by common corners leaving one-dimensional cavities occupied by the tetrahedron chains.

The comparison with the maghemite and hematite structures shows many intermediate features in ε-Fe_2O_3. The anion arrangement, double-hexagonal, the fraction of four-coordinated iron (25%), and the volume per formula unit (5.29×10^6 pm^3 vs 5.46×10^6 and 5.04×10^6 pm^3 in γ- and α-Fe_2O_3, respectively) are intermediate. As in hematite, all oxygen sandwiches contain the same amount of iron, 0.67

TABLE 3
Structural Characteristics of ε-Fe_2O_3

$a = 509.5(1)$ pm $\quad b = 878.9(2)$ pm $\quad c = 943.7(3)$ pm
$V = 423 \times 10^6$ pm^3 $\quad$ Content: $Fe_{16}O_{24}$
Space group: $Pna2_1$-C_{2v}^9

Idealized positions

O_1	$0\ 0\ 0$		O_2	$0\ \frac{1}{3}\ 0$		O_3	$0\ \frac{2}{3}\ 0$
O_4	$\frac{1}{6}\ \frac{1}{2}\ \frac{1}{4}$		O_5	$\frac{1}{6}\ \frac{5}{6}\ \frac{1}{4}$		O_6	$\frac{1}{6}\ \frac{1}{6}\ \frac{1}{4}$
Fe_1	$\frac{1}{3}\ \frac{1}{3}\ \frac{1}{8}$		Fe_2	$\frac{1}{3}\ 0\ \frac{3}{8}$		Fe_3	$\frac{1}{3}\ \frac{2}{3}\ \frac{3}{8}$
Fe_4	$\frac{1}{6}\ \frac{1}{6}\ \frac{1}{16}$						
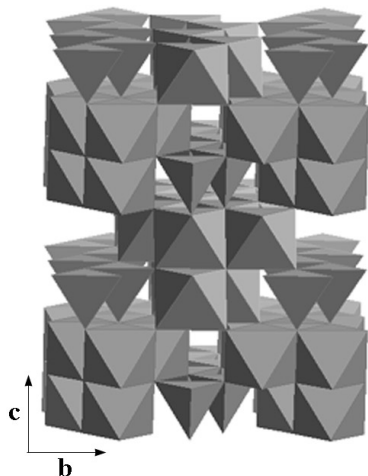
FIG. 8. Polyhedral representation of the structure of ε-Fe₂O₃.

TABLE 4
Lattice Constants of Isomorphous Materials

	a (pm)	b (pm)	c (pm)
κ-Al₂O₃ (20)	484	833	895
AlFeO₃ (17)	497	860	925
ε-Ga₂O₃[a]	503	871	930
GaFeO₃ (18)	507	875	940
ε-Fe₂O₃	510	879	944

[a] Deduced from ref. (22)

Fe per O atom. As in maghemite, oxygen sandwiches containing six-coordinated iron alternate with sandwiches containing six- and four-coordinated iron, but in the latter sandwiches only one of the two layers of tetrahedral sites is now occupied. Thus, in some sense, ε-Fe₂O₃ may be viewed as intermediate between γ- and α-Fe₂O₃.

(c) Isomorphous materials. The structure of ε-Fe₂O₃ determined herein is similar to that of GaFeO₃ (16, 17). In GaFeO₃, gallium fills the tetrahedral site and essentially shares the Fe₃ octahedral site with iron (named Ga₁ and Ga₂, respectively, in ref (16), Fe₁ and Fe₂ keeping the same label). In Table 1 are reported the XRD line intensities calculated for ε-Fe₂O₃ using the atomic positions in Ga$_{0.87}$Fe$_{1.13}$O₃ (16) deduced from single-crystal refinement. The corresponding schematic pattern ($b/a = \sqrt{3}$) is shown in Fig. 6d. The good agreement with the observed data clearly supports our simple analysis.

GaFeO₃ is isostructural with AlFeO₃ and, as a matter of fact, the XRD pattern of ε-Fe₂O₃ resembles that of AlFeO₃ (18). The structures of GaFeO₃ and AlFeO₃ have generally been described using the ($c < a < b$) orientation of the unit cell, leading to space group $Pc2_1n$. For the sake of clarity, we have adopted the ($a < b < c$) orientation where the c axis is common to the orthorhombic and hexagonal cells, leading to space group $Pna2_1$. κ-Al₂O₃ is isomorphous. This was debated (19) but is now undoubted in view of the structural determination (20) published recently. The lattice constants of the four compounds are listed in Table 4. The variations between the materials follow the variation of the cation ionic radius (Al^{3+} < Ga^{3+} < Fe^{3+}) (21). ε-Ga₂O₃ is presumably isomorphous, as suggested by the XRD pattern (22) that can be indexed on an orthorhombic unit cell with symmetry C_{2v}^9 and parameters fitting in with the aforementioned series (Table 4). These remarks clearly focus on a common structure type of the iron, aluminum, and gallium

sesquioxides. Mixed gallium or aluminum iron oxides, Ga(Al)$_{2-x}$Fe$_x$O₃, have been reported for limited ranges of stoichiometric composition, with about $0.8 < x < 1.2$ for gallium and $0.6 < x < 1.0$ for aluminum (23, 24). Our results suggest the possible formation of an extensive range of solid solutions from Ga(Al)₂O₃ to Fe₂O₃.

(d) Order–disorder relationship. The common structural features of the ordered [4] and disordered [1] structures in addition to the cell–subcell relationship and the characteristics of the diffuse scattering (see Section 2a) strongly suggest an order–disorder relationship between the cation arrangements. Two types of disorder may be considered. On the one hand, because the ordered arrangement can take six different orientations with respect to the oxygen stacking, a domain structure may occur at short range. On the other hand, the site occupancy may be disordered, which is inevitable in the case of significant departure, in either way, from the 1:3 stoichiometry of the four- to six-coordinated iron. This kind of disorder induces face sharing between tetrahedra and octahedra or between octahedra. The avoidance of such situations is likely to bring correlations between the site occupancies that maintain the order locally. We may reasonably assume that both types of disorder, site occupancy and orientation, manifest themselves in a similar way regarding the symmetry of the average unit cell relevant to powder diffraction. Considering the symmetry ($mm2$) of the ordered structure and close-packing requirements, the possible point groups are $6/mmm$ ($\bar{6}m2$), $6mm$, and $3m$, with the possible space groups being limited to $P6_3/mmc$, $P6_3mc$, and $P\bar{3}m1$. $P\bar{3}m1$ is excluded, which tends to support our conclusion in favor of the model with symmetry $P6_3mc$ [2] for fitting the data of Dézsi and Coey (7).

According to our results, the fraction of four-coordinated iron in disordered ε-Fe₂O₃ (40%) is larger than in ordered ε-Fe₂O₃ (25%) and similar to that found in γ-Fe₂O₃ (37.5%). Such a feature, which is presumably related to the lack of order at long range, actually needs to be confirmed. However, we can reasonably conclude that the variations in the XRD line intensities observed (Table 1) between the various ε-Fe₂O₃ materials are due to different degrees of

cation ordering, possibly because of different stoichiometries of four- and six-coordinated iron.

3. Mössbauer Spectroscopy

Mössbauer spectra of the composite without and with a longitudinal external magnetic field of 6 T are shown in Fig. 9.

(a) Zero-field spectra. The spectrum at 293 K in zero applied field is complex. A first approximation leads us to consider five sextets. The fit results are reported in Table 5. The sextet with the largest hyperfine field (identical to the effective field in zero applied field) is ascribed unambiguously to hematite. The other four components characterize the spectrum of ε-Fe_2O_3. Their relative areas are similar, indicating four sites with equal occupancies, assuming that all iron atoms in ε-Fe_2O_3 have the same recoilless fraction. The values of the isomer shift, IS, indicate three octahedral

sites and one tetrahedral site. This suggests the assignment of each component to a definite crystallographic site. Two octahedral sites are characterized by similar values (~ 45 T) of the hyperfine field, H_{hyp}, and different values of the quadrupole shift, QS. The third site exhibits a smaller hyperfine field (~ 40 T). Both H_{hyp} values are smaller than for hematite and maghemite (~ 50 T) but remain classical for Fe^{3+}-based oxides. In contrast, the value (26 T) deduced from the magnetic splitting of the tetrahedral component is unusually low.

At 80 K, the magnetic splitting of the ε-Fe_2O_3 components is strongly increased, particularly that of the tetrahedral component. Due to strong overlap of the octahedral components, the spectrum could be fitted satisfactorily with up to four sextets, one being ascribed to tetrahedral sites and the others to octahedral sites (Table 5). The sextet with the largest H_{hyp} value still corresponds to hematite. The positive quadrupole shift indicates that the Morin transition has occurred. However, the QS value is twice as small as expected for bulk hematite. This may indicate that only a part of the hematite has undergone the transition but may also be an artifact of the fit due to the component overlap. The ratio of the total octahedral to tetrahedral ε-Fe_2O_3 spectral areas is 3:1 as at 293 K. The ratio of the ε- to α-Fe_2O_3 spectral areas is larger than at 293 K.

(b) In-field spectrum. Under 6 T at 9 K, the lines at high velocity ($\sim \pm 8$ mm/s) split, showing that ε-Fe_2O_3 is a ferrimagnet. The large relative area of the lines at medium velocity ($\sim \pm 5$ mm/s) indicates that it is canted under the experimental conditions.

The magnetic splitting is given by the effective magnetic field at the ^{57}Fe nucleus, defined by $\mathbf{H}_{eff} = \mathbf{H}_{hyp} + \mathbf{H}_{app}$,
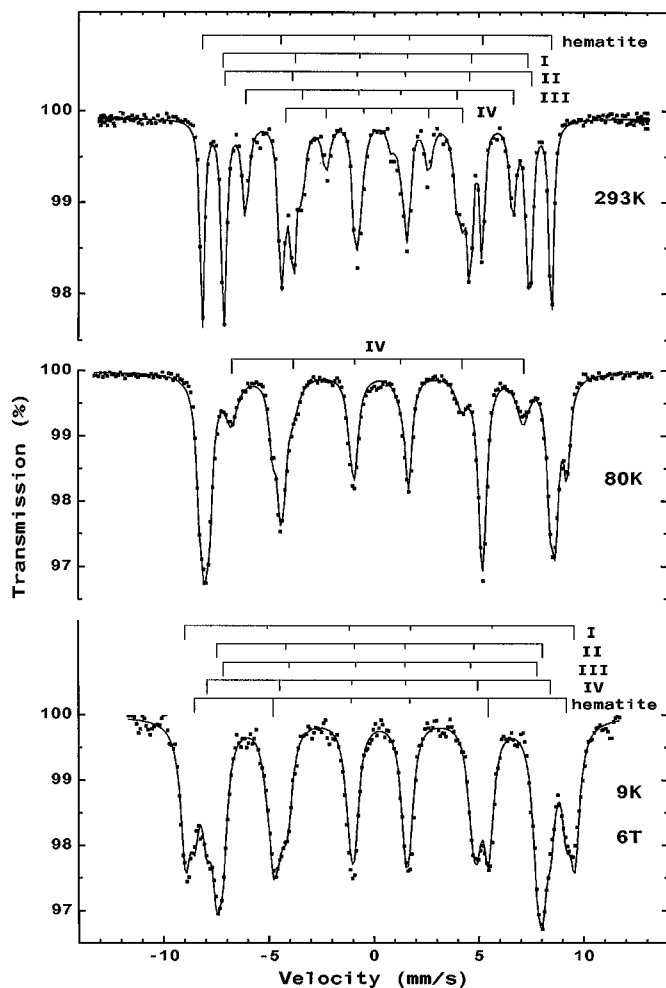

FIG. 9. Mössbauer spectra of the ε-Fe_2O_3/silica composite in zero applied magnetic field and in a longitudinal field of 6 T.

TABLE 5
Fitted Mössbauer Parameters

		A (%)	IS (mm/s)	QS (mm/s)	H_{eff} (T)	Γ (mm/s)	q
293 K		29	0.37(1)	−0.11(1)	51.5(1)	0.24(1)	
$H_{app} = 0$		17	0.37(1)	−0.19(1)	45.0(1)	0.24(1)	
		17	0.39(1)	−0.06(1)	45.2(1)	0.24(1)	
		19	0.38(1)	−0.00(1)	39.5(1)	0.37(1)	
		18	0.21(1)	−0.07(1)	26.2(1)	0.42(2)	
80 K		21	0.47(1)	0.11(1)	54.2(1)	0.39(1)	
$H_{app} = 0$		32	0.45(1)	−0.03(1)	51.8(1)	0.39(1)	
		27	0.47(1)	−0.05(1)	50.3(1)	0.39(1)	
		20	0.30(1)	−0.01(1)	43.1(1)	0.71(2)	
9 K	I	20	0.46(1)	0.02(1)	57.4(1)	0.53(5)	0.6(3)
$H_{app} = 6$ T	II	20	0.46(2)	−0.02(2)	48.1(2)	0.48(14)	1.2(5)
	III	19	0.47(2)	−0.01(2)	46.3(3)	0.51(7)	1.2(3)
	IV	20	0.39(1)	0.00(1)	50.6(2)	0.55(10)	2.2(4)
	V	21	0.49(1)	0.00(1)	54.8(2)	0.51(9)	4.1(5)

[a] A stands for the relative area, IS the isomer shift, QS the quadrupole shift, H_{eff} the effective magnetic field, and Γ the line width. Sextet lines with relative areas in the ratios $3:q:1:1:q:3$ ($q = 2$ for $H_{app} = 0$).

where $\mathbf{H}_{hyp}$ is the hyperfine field and $\mathbf{H}_{app}$ the applied field. The hyperfine field is proportional to the magnetic moment of the cation and oriented in the opposite direction. The line areas in a sextet are in the ratios $3:q:1:1:q:3$ with $q = 4\sin^2\varphi/(1 + \cos^2\varphi)$, where φ is the angle between $\mathbf{H}_{eff}$ and the γ-ray ($\mathbf{H}_{app}$) direction. Thus, $q = 0$ if alignment parallel or antiparallel to the applied field is achieved, and $q = 4$ for a perpendicular orientation such as in antiferromagnets. An orientation at random over $(0, \pi/2)$, $(\pi/2, \pi)$, or $(0, \pi)$ leads to $q = 2$.

The in-field spectrum was fitted with five independent sextets. The fit results are reported in Table 5. The q values range from 0.6 to 4. The component with $q = 4$ (V) is ascribed to hematite. Its relative area is the same as at 80 K. The other components have similar relative areas and show IS values suggesting attribution to three octahedral sites (I–III) and one tetrahedral site (IV). These components are therefore assigned to ε-Fe₂O₃.

The comparison of the relative areas of the hematite and ε-Fe₂O₃ components in the three spectra suggests that all iron atoms in ε-Fe₂O₃ have a similar recoilless fraction, f_ε, which is similar to the recoilless fraction, f_α, in hematite at 9 and 80 K and smaller than f_α at 293 K. The decrease of the f_ε/f_α ratio at high temperature indicates enhanced vibrations in ε-Fe₂O₃. This may result from a smaller Debye temperature than that of hematite or from vibrations of the ε-Fe₂O₃ particles (much lighter than the hematite ones) in conjunction with changes in the elastic properties of the matrix. The low-temperature data suggest that the ε-Fe₂O₃ phase involves ca. 80% of the iron in the composite.

The orientation and magnitude of the hyperfine fields in ε-Fe₂O₃ at 9 K under 6 T deduced from the fitted parameters are reported in Table 6. The hyperfine field at octahedral site I is canted at ca. 35°. The hyperfine fields at sites II and III are parallel to each other and are canted in the opposite direction at approximately the same angle. The hyperfine field at the tetrahedral site (IV) is canted at ca. 65°. The situation, illustrated in Fig. 10, suggests a ferrimagnetic structure with three (or four) sublattices, I, (II, III), and IV. Assuming a magnetic moment of 5 μ_B per Fe³⁺ ion, we deduce a net magnetization of 0.4 μ_B per Fe under 6 T. This small value, approximately three times less than for γ-
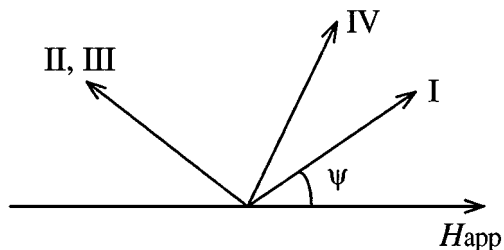

FIG. 10. Orientation of the hyperfine field in ε-Fe₂O₃ at 9 K under 6 T.

Fe₂O₃, seems consistent with magnetic data (6, 8). Note that due to strong overlap of the components and possible distributions of orientation, the interpretation of the spectrum may not be unique. In particular, the situation where the hyperfine field at the tetrahedral sites is randomly oriented over $(0, \pi/2)$ cannot be discarded firmly.

(c) Magnetic structure. The iron ions interact magnetically with near neighbors via Fe–O–Fe superexchange bonds. Roughly speaking, there are three types of Fe–O–Fe bonds in the structure (Fig. 7 and Table 4), namely bonds at an angle close to 180°, which are strongly antiferromagnetic, bonds at an angle of the order of 120°, which are also antiferromagnetic but less strong, and bonds at an angle close 90°, which are only weakly magnetic. An Fe₁ ion interacts with four Fe₂ ions through one 180° bond and three 120° bonds and with two Fe₃ ions through one 180° bond and one 120° bond, and vice versa. An Fe₄ ion interacts with cations of each type, in varying number, through bonds at ca. 120°. All remaining bonds are at ca. 90° or nonexisting. Therefore, the major magnetic features are a strong antiferromagnetic coupling between Fe₁ and (Fe₂, Fe₃) and frustrated antiferromagnetic interactions at Fe₄. Thus, we may expect a (nearly) collinear ferrimagnetic order at the octahedral sites and lack of alignment, with possible disorder, at the tetrahedral sites. Note that the antiferromagnetic coupling should be weaker at Fe₃ than at Fe₂ due to a weaker reinforcement from the 120° bonds.

These features are fully consistent with the analysis of the in-field Mössbauer spectrum (Table 6) and lead us to identify site I with Fe₁, site III, which presents the smallest hyperfine field among the octahedral sites, with Fe₃, and, consequently, site II with Fe₂. The fact that the Fe₁ and (Fe₂, Fe₃) moments are canted under the experimental conditions suggests a large anisotropy energy and the requirement of much higher fields for achieving the alignment. The magnetic behavior at the octahedral sites is somewhat similar to that observed in GaFeO₃ (17, 23). GaFeO₃ is a collinear ferrimagnet with two sublattices, Fe₁ and (Fe₂, Fe₃), the tetrahedral sublattice occupied by gallium being nonmagnetic. An applied field of 9 T is necessary to obtain alignment at 4.2 K (23). The easy direction of magnetization is the *a* direction ($a < b < c$ orientation). Studies (24) of

TABLE 6
Canting Angles in ε-Fe₂O₃ at 9 K under 6 T[a]

Site	φ (deg)	H_{hyp} (T)	ψ (deg)
I	31 ± 8	52.5	33 ± 9
II	138 ± 9	52.5	143 ± 8
III	138 ± 6	51.0	144 ± 8
IV	57 ± 5	47.5	63 ± 6

[a] φ stands for the canting angle of the effective field, and ψ for that of the hyperfine field, of magnitude H_{hyp} (± 0.5 T).

oriented samples in the paramagnetic state showed that the symmetry axis of the electric field gradient tensor at the nucleus is inclined with respect to the easy direction at an angle $\zeta \sim 90°$ at the Fe_1 site and $\sim 55°$ at the Fe_2 site. In the magnetic state in zero applied field, the quadrupole shift is proportional to $(3 \cos^2 \zeta - 1)$. Thus, we may expect $QS \neq 0$ at Fe_1 and $QS \sim 0$ at Fe_2. Assuming a similar situation in ε-Fe_2O_3, among the two octahedral components with $H_{hyp} = 45$ T at 293 K (Table 5), we attribute the one with $QS = -0.19$ mm/s to Fe_1 and that with $QS = -0.06$ mm/s to Fe_2, the octahedral component with smaller hyperfine field being ascribed to Fe_3 and the tetrahedral one to Fe_4, which completes the line assignment in the 293 K spectrum.

The magnetic moment at the tetrahedral site exhibits a particular thermal behavior. The H_{hyp} value (Tables 5 and 6) deduced from the magnetic splitting decreases by ca. 45% as the temperature increases from 9 to 293 K. The reduction is only ca. 20% at Fe_3, 15% at Fe_1 and Fe_2, and 6% in hematite. The rather low Curie temperature (~ 480 K) (4, 6) of ε-Fe_2O_3 can presumably explain the difference between the thermal effects at (Fe_1, Fe_2) and in hematite but certainly not the large effect observed at the tetrahedral site. This suggests that the Fe_4 moments, which are rather weakly coupled to their neighbors, undergo dynamical phenomena. Such phenomena may also affect the Fe_3 moments and ε-Fe_2O_3 should actually be considered a four-sublattice ferrimagnet. Further investigations of the phenomena are in progress.

CONCLUSION

We clearly confirmed the existence of ε-Fe_2O_3. We established that it is isomorphous with $GaFeO_3$, $AlFeO_3$, κ-Al_2O_3, and presumably ε-Ga_2O_3. Like the gallium or aluminum iron oxides, ε-Fe_2O_3 is probably piezoelectric. It is a noncollinear ferrimagnet, with the tetrahedral sublattice exhibiting a particular thermal behavior.

ε-Fe_2O_3 appears to be intermediate between γ-Fe_2O_3 and α-Fe_2O_3 in several structural respects, in particular regarding the anion arrangement, the fraction of four-coordinated cations, and the volume per formula unit. The formation of ε-Fe_2O_3 by heat treatment of γ-Fe_2O_3 particles well dispersed in silica is related to the limited agglomeration of γ-Fe_2O_3 particles that can take place in a certain temperature range, extended agglomeration leading, as in powders, straight to α-Fe_2O_3. γ-Fe_2O_3 particles are stable against heat as long as the matrix or a surface coating prevents them from sintering. Sintering causes transformation into ε-Fe_2O_3 or α-Fe_2O_3 depending on the degree of agglomeration, that is, depending on growth limitations of the product phase. These features focus on the role of space confinement conditions in stabilizing metastable phases and suggest the possible formation of other unusual polymorphs under such conditions.

REFERENCES

1. C. Chanéac, E. Tronc, and J. P. Jolivet, *Nanostruct. Mater.* **6,** 715 (1994).
2. C. Chanéac, E. Tronc, and J. P. Jolivet, *J. Mater. Chem.* **6,** 1905 (1996).
3. H. Forestier and G. Guiot-Guillain, *C. R. Acad. Sci.* (*Paris*) **199,** 720 (1934).
4. R. Schrader and G. Büttner, *Z. Anorg. Allg. Chem.* **320,** 220 (1963); Powder Diffraction File No. 16-653, JCPDS-International Center for Diffraction Data, Swarthmore, PA, 1993.
5. L. Walter-Lévy and E. Quémeneur, *C. R. Acad. Sci.* (*Paris*) **257,** 3410 (1963); Powder Diffraction File No. 16-895, JCPDS-International Center for Diffraction Data, Swarthmore, PA, 1993.
6. J. M. Trautmann and H. Forestier, *C. R. Acad. Sci.* (*Paris*) **261,** 4423 (1965).
7. I. Dézsi and J. M. D. Coey, *Phys. Status. Solidi. A* **15,** 681 (1973).
8. N. Viart, Thesis, Univ. Strasbourg, 1996; J. L. Dormann, N. Viart, J. L. Rehspringer, A. Ezzir, and D. Niznansky, *Hyperfine Interact.* **112,** 89 (1998).
9. J. P. Jolivet and E. Tronc, *J. Colloid Interface Sci.* **125,** 688 (1988).
10. P. Prené, E. Tronc, J. P. Jolivet, J. Livage, R. Cherkaoui, M. Noguès, J. L. Dormann, and D. Fiorani, *IEEE Trans. Magn.* **29,** 2658 (1993).
11. C. Boudias and D. Manceau, CaRine Crystallographie v.3.0 (1989–1996), Divergent S.A., Compiègne, France.
12. D. R. Dasgupta, *Indian J. Phys.* **35,** 401 (1961).
13. R. A. Eggleton and R. W. Fitzpatrick, *Clays Clay Miner.* **36,** 111 (1988).
14. K. Haneda and A. H. Morrish, *Solid State Commun.* **22,** 779 (1977).
15. "International Tables for X-Ray Crystallography," Vol. I, Kynoch Press, Birmingham, U.K., 1969.
16. S. C. Abrahams, J. M. Reddy, and J. L. Bernstein, *J. Chem. Phys.* **42,** 3957 (1965).
17. E. F. Bertaut, G. Bassi, G. Buisson, J. Chappert, A. Delapalme, R. Pauthenet, H. P. Rebouillat, and R. Aleonard, *J. Phys.* (*Paris*) **27,** 433 (1966).
18. Powder Diffraction File No. 30-24, JCPDS-International Center for Diffraction Data, Swarthmore, PA, 1993.
19. R. R. Dayal, J. A. Gard, and F. P. Glasser, *Acta Crystallogr.* **18,** 574 (1965).
20. B. Ollivier, R. Retoux, P. Lacorre, D. Massiot, and G. Férey, *J. Mater. Chem.* **7,** 1049 (1997).
21. R. D. Shannon and C. T. Prewitt, *Acta Crystallogr. Sect. B* **25,** 925 (1969).
22. R. Roy, V. G. Hill, and E. F. Osborn, *J. Am. Chem. Soc.* **74,** 719 (1952); Powder Diffraction File No. 6-509. JCPDS-International Center for Diffraction Data, Swarthmore, PA, 1993.
23. M. Schieber, R. B. Frankel, N. A. Blum, and S. Foner, *J. Appl. Phys.* **38,** 1282 (1967).
24. J. M. Trooster and A. Dynamus, *Phys. Status Solidi* **24**, 487 (1967).